Meteorol. Atmos. Phys. 76, 83–105 (2001)

Meteorology
and Atmospheric
Physics

[1] Institute for Fruit and Vegetable Production, University of Bonn, Bonn, Germany
[2] Meteorological Institute, University of Bonn, Bonn, Germany

An integrated approach for the determination of regional evapotranspiration using mesoscale modelling, remote sensing and boundary layer measurements

P. Braun[1], **B. Maurer**[2], **G. Müller**[2], **P. Gross**[2], **G. Heinemann**[2], and **C. Simmer**[2]

With 24 Figures

Received January 28, 2000
Revised June 24, 2000

Summary

A method is presented for the calculation of regional evapotranspiration by means of mesoscale modelling using the "Lokal-Modell" (LM) of the German Weather service with 2.8 km horizontal resolution. The shortcomings of the model with respect to the quantitative simulation of cloudiness and precipitation are overcome by the assimilation of precipitation and insolation (derived by radar and METEOSAT data, respectively) into the SVAT module of the LM. Three case studies are presented in order to quantify the influence of the assimilation on the simulated evapotranspiration process. The simulations are validated using ground-based measurements of surface layer quantities, turbulent fluxes and boundary layer structures. Different methods for the determination of the turbulent flux of latent heat are intercompared. Simulated surface energy fluxes are strongly influenced by the assimilation, which highly improves the results for the evapotranspiration field in the case of a strong rain event. The validation studies for cases under fair weather conditions show large uncertainties in the simulated energy fluxes. The sensitivity with respect to the soil moisture content is investigated. An artificially increased soil moisture results in a significantly better representation of the turbulent fluxes in the LM, but the agreement with simultaneously measured boundary layer structures is reduced.

1. Introduction

Evapotranspiration is one of the most fundamental processes, which influence climate and weather from the local to the global scale. Evapotranspiration is always interlocked with the other components of the surface energy balance, mostly the net radiation absorbed at the surface. Thus evapotranspiration closely links the energy cycle of our climate system with hydrology. As a typical exchange process evapotranspiration is governed by the state of both the atmosphere and the earth's surface. While the atmosphere controls its moisture mainly by turbulent transport of water vapour from the surface to the free atmosphere and by providing water to the surface through the precipitation process, the availability of water for the evaporation process from the earth's surface is dependent on stomatal control of transpiration and soil water transport properties. Because both regimes, atmosphere and the earth's surface, operate on very different time and space scales, evapotranspiration exhibits very complex spatial and temporal patterns, which make the determination of regional fields an ambitious task.

There is a range of techniques to determine evapotranspiration by in situ measurements. The Bowen ratio method (Bowen, 1926) links the measured gradients of temperature and specific humidity to the corresponding turbulent fluxes of sensible and latent heat; the turbulent fluxes are parameterized by the gradient of the quantity being transported according to the K- (or Austausch-) theory. A direct method is given by the eddy covariance method based on direct measurements of the turbulent transfer process (e.g., Foken and Wichura, 1996). These techniques, however, are very cost intensive and, consequently, measurements only at selected points in time and space are possible. Airborne measurements using eddy correlation can be used to extrapolate the point measurements to a larger area, but these measurements are even more costly and can thus give only a glimpse of regional evapotranspiration.

Satellite measurements are frequently used to determine the turbulent energy fluxes at regional scales (e.g., Pelgrum and Bastiaanssen, 1996). Most of these methods take advantage of the measurements of solar reflection and thermal emission of the surface-atmosphere system. Eymard and Taconet (1995) give a very general overview of these and other techniques. The simplest procedures derive statistical relationships between passive microwave measurements and evaporation. Other methods determine evaporation as a residuum of the surface energy balance. For that purpose the net radiation is estimated from measurements in the visible channel and the sensible heat flux with a combination of remotely sensed and in-situ measurements. A third method is based on the assimilation of satellite data into a SVAT (Soil-Vegetation-Atmosphere Transfer) model. The validation experiments of Eymard and Taconet (1995) demonstrate that the above techniques are not able to calculate evaporation with acceptable accuracy. Most of the methods are basically tuned to describe evaporation of soil water and therefore fail if the land surface is covered by vegetation. The main disadvantage, however, is that the crucial role of the atmosphere, as described above, and its inherent spatial and temporal scales are almost totally neglected.

High-resolution dynamic atmosphere models coupled with SVAT schemes driven with appropriate observations, which put emphasis on the parameters controlling evapotranspiration, are currently the best source of information about the actual state of the atmosphere on the relevant scales. A major problem, however, is the lack of highly resolved observations to initialize these models. In addition, there are still problems to simulate convection, cloudiness and rainfall adequately on this scale. These processes, however, influence the surface energy balance through radiation and the availability of soil moisture. In this study we mitigate these problems by using observed precipitation fields from radar and observed cloud fields from satellite. This information is used to determine the solar radiation actually absorbed by the surface and the source of soil moisture as input for a SVAT module, which is coupled to a mesoscale dynamic atmospheric model.

Validation of such a coupled model needs validation on all relevant scales. Our goal is the implementation of a validation system reaching from (a) local flux measurements and measurements of tree transpiration to extrapolate evapotranspiration measurements to the scale of e.g., large fruit orchards or forests, (b) aircraft and boundary layer measurements to cover areas with extensions of several tens of kilometres and the whole boundary layer, to (c) satellite observations of the surface radiation temperature for the largest spatial scale (Fig. 1). Finally, the model should be coupled to a hydrological model to validate the water balance on larger time scales. Only part of the validation chain has been implemented yet, in particular the local energy balance measurements, the measurements of tree transpiration and – for selected periods – boundary layer measurements, about which we will report here in particular.

The study aims specifically at the determination of the spatial and temporal variability of evapotranspiration over the "Niederrheinische Bucht"

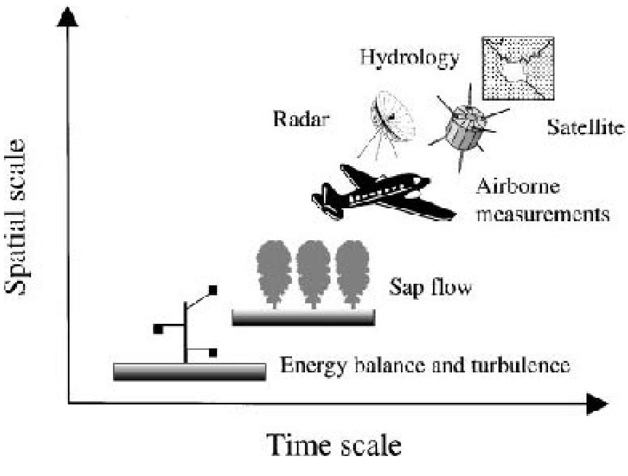

Fig. 1. Schematic representation of time and spatial scales of available methods to validate simulated regional fields of evapotranspiration

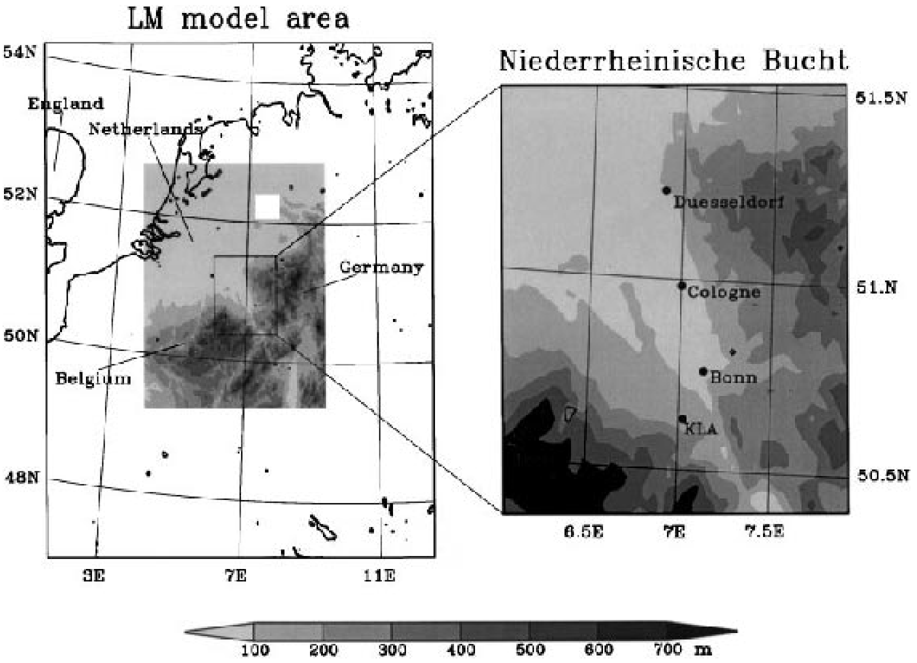

Fig. 2. Location of the LM-model area (shaded domain in the left picture) and topography of the Niederrheinische Bucht (NRB). Point KLA (Klein-Altendorf) indicates the location of the field measurement site

(NRB). In the scope of this paper, NRB extends from the Belgium border in the west to about 50 km east of Bonn, and from 30 km south of Bonn to Düsseldorf in the north (Fig. 2). We use the "Lokal-Modell" (LM) (Doms and Schättler, 1999) of the German Weather Service (DWD) to represent the state of the atmosphere. Figure 2 shows on the left the domain of the LM, which reaches from the Dutch coast in the northwest to the upper Rhine valley in the southeast. In order to improve the evapotranspiration calculated by the SVAT module TERRA in the LM, precipitation from the German radar network of the DWD and cloud information from METEOSAT data are used to drive the SVAT module. The model results are validated by ground-based measurements of the fluxes and the state of the atmospheric boundary layer. Both profile and direct turbulence measurements were carried out during an intensive observation period in summer 1998.

The paper is organized as follows: First the mesoscale atmospheric model is described (Sect. 2). Then, data and methods used are presented in Sect. 3, followed by the description of assimilation results in Sect. 4. Section 5 covers the validation results before we conclude with a summary and an outlook in Sect. 6.

2. Mesoscale model

The model used is the "Lokal-Modell" (LM), which is a part of the operational numerical weather prediction system of DWD since December 1999. It is based on the primitive equations. Due to its non-hydrostatic nature, the LM is suitable for the prediction of atmospheric flow systems down to the meso-γ scale. The prognostic variables are the three dimensional wind-vector, temperature, perturbation pressure, specific humidity, cloud water content and, optionally, cloud ice content as well as turbulent kinetic energy. The variables are treated on a staggered rotated geographical grid of Arakawa C-type with a grid size of 2.8 km. In the vertical dimension the equations are formulated in a generalized terrain following coordinate. The number of vertical layers amounts to 35 with 10 layers being arranged below 1500 m above ground.

In our test cases, we use a pre-operational version of the LM (V1.17). This version starts with an interpolated analysis of the hydrostatic "Deutschland-Modell" (DM), which was the operational numerical weather prediction model of the DWD for the meso-β-scale until 30 November 1999. The lateral boundary values are provided either by a DM forecast at hourly intervals (operational mode) or by subsequent DM analyses (analysis mode). The lateral boundary formulation is according to Davies (1976).

The parameterizations of the LM include a subgrid-scale turbulence scheme with a diagnostic second order closure for vertical turbulent fluxes following Mellor and Yamada (1974). The surface layer is parameterized by stability and roughness-length dependent formulations of momentum, heat and moisture fluxes according to the similarity theory after Louis (1979). A representation of cloud microphysics as well as a mass flux scheme for moist convective processes developed by Tiedtke (1989) are also implemented. The effects of short-and longwave radiation fluxes are calculated by a δ-two-stream approximation of the radiative transfer equation according to Ritter and Geleyn (1992). Radiation is computed every 30 min.

In the scope of the present study the parameterization of soil processes is of special interest. The coupling of atmosphere and pedosphere is defined by the energy balance equation. In order to calculate the energy balance, surface temperature and specific humidity at ground level need to be quantified. The value of these quantities is the main output of the soil model TERRA, which is separated into a hydrological and a thermal part.

In the hydrological section the water content of various stores at the surface and in the underlying soil is calculated. TERRA includes an interception store, a snow store and two layers of soil. The hydrological coupling of soil and atmosphere contains precipitation, rime and dew as sources, and evaporation, transpiration and runoff as sinks of soil water. Evaporation from bare soil is derived as a function of soil texture and soil moisture. Transpiration by plants depends on soil water content, rooting depth and soil texture. A more comprehensive description of vegetation taking, for instance, the leaf area index into account is not yet implemented. The soil water content is predicted by simple budget equations for the soil layers. Exchange and transport of water between stores includes processes such as infiltration, percolation and capillary ascent. The vertical water transport in the soil is formulated according to the Darcy equation. The runoff is calculated for each layer but lateral transport of water between neighbouring soil columns is not accounted for.

The thermal part provides a forecast of surface temperature and temperature at the interface between upper and lower soil layer in a two-layer model by solving the equation of heat conduction. At the transition between second soil layer and deep soil the temperature is held constant. The temperature budget of the soil is forced by various energy fluxes. Atmospheric forcing is given by net radiation flux and the turbulent fluxes of heat and moisture. Calculation of soil layer thicknesses and of soil heat fluxes is based on the Extended Force Restore (EFR) method (Jacobsen and Heise, 1982). Assuming atmospheric forcing to be a harmonic function in time, the EFR method solves the equation of heat conduction exactly. The EFR method determines adequate layer depths as well as heat fluxes in the soil as functions of thermal conductivity and heat capacity. These and a number of other parameters depend on soil texture. TERRA distinguishes between five different standard soil types (sand, sandy loam, loam, loamy clay and clay) and three special types (ice, rock and peat). More detailed information about the LM can be found in Doms and Schättler (1999).

3. Material and methods

3.1. Synoptic overview over the case studies

To evaluate the effects of either assimilating remotely sensed data into the LM via the TERRA module or to compare it with ground-based measurements, three periods have been chosen for case studies. The general weather situations for these periods are described below using DM analyses.

The first case study, 4 July 1994, represents a strong rainfall event. In the first few days of July 1994 Central Europe had experienced mostly cloud free days. During 3 July 1994 a low pressure system developed over the northern part of France and moved to north Germany on 4 July (Fig. 3a). Around local noon the cold front of the system associated with a squall-line crossed the NRB area and caused a fall in temperature from 35 °C in front of to 25 °C behind the front. Heavy thunderstorms and occasional hail were observed with the passage of the squall-line. In the vicinity of Cologne, the 12-hourly rainfall measurements amounted to about 40 mm.

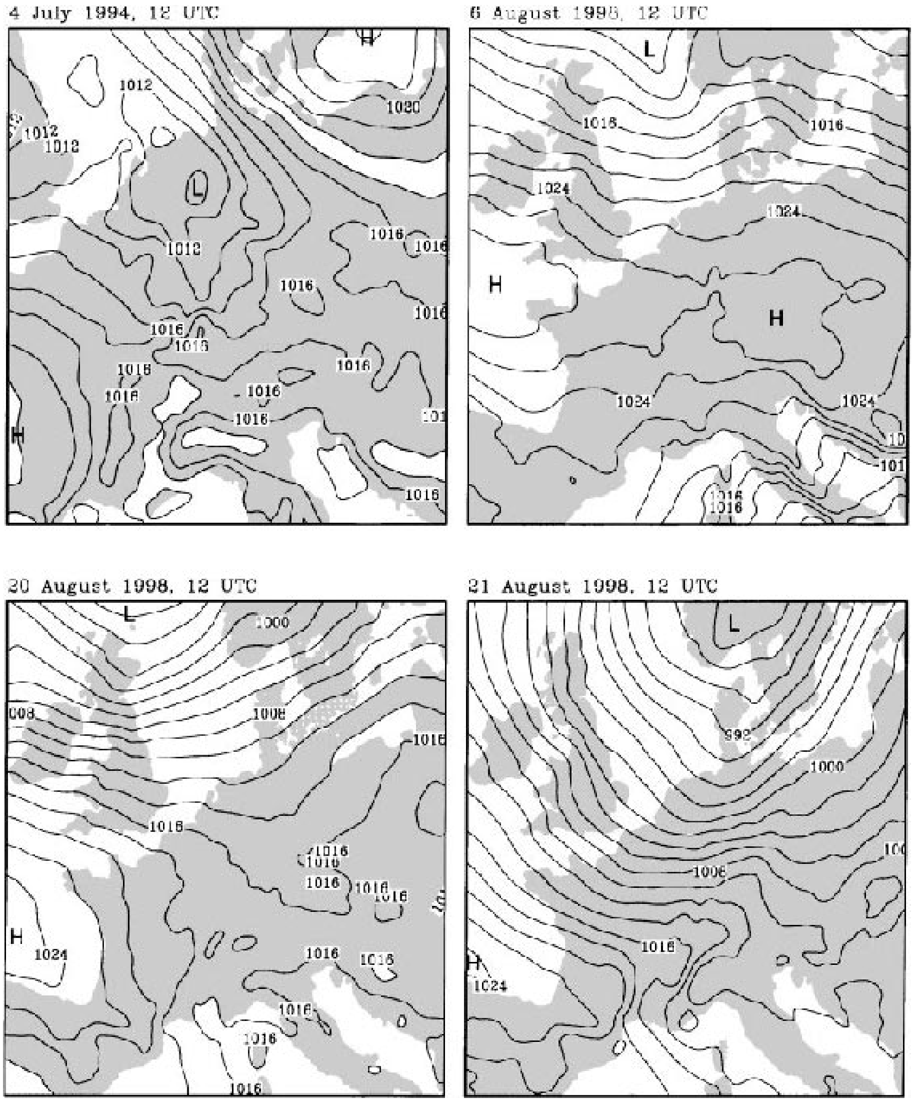

Fig. 3. Sea-level pressure in hPa from the operational DM-analyses for **a** 4 July 1994 12 UTC; **b** 6 August 1998 12 UTC; **c** 20 August 1998 12 UTC; **d** 21 August 1998 12 UTC; contour interval: **a** 1 hPa, **b–d** 2 hPa. Areas of low and high pressure are indicated by L and H, respectively. Note: the DM-domain was enlarged since 1997

For case study 2, a calm summery weather situation around 6 August 1998 was selected. After a cold front had crossed Germany on 4 August, a high pressure ridge expanded from the high pressure centre west of the Channel to Central Europe. The sea-level pressure map of 6 August 1998 12 UTC (Fig. 3b) shows only weak pressure gradients in the NRB region. Due to relatively cold air in the middle troposphere cumulus clouds developed in the course of the morning hours especially in the mountainous areas of NRB. The warm front of a low pressure system, which was located over the North Sea and moved to Scandinavia, only influenced the coastal regions of Germany.

The third case study covers the period from 19 to 21 August 1998. During this period the NRB area was mainly influenced by a large low pressure system, which moved from Iceland to Scandinavia. The weather situation of 19 August was characterized by weak pressure gradients in Central Europe with some cumulus clouds over the NRB mountains. While the morning of 20 August (Fig. 3c) was still sunny, clouds grew in the course of the day due to a weak upper level cold front, which crossed NRB during the night. This front was accompanied by only minor rain. On 21 August a second frontal system associated with a large surface trough extending from the south of Scandinavia to the northwest of France reached NRB (Fig. 3d). Thunderstorms and heavy rain showers developed in the convergent flow of the cold front.

The convective case of 4 July 1994 is highly suited for demonstrating the influence of assimilating satellite and radar information into the

SVAT module of LM (see Sect. 3.2). Unfortunately evaporation measurements at our measurement site KLA (Fig. 2) started not before 1998, so that a validation of the LM evaporation forecast could not be performed. For cases two and three measurements of the surface energy balance and of the boundary layer structure are available for the model validation. In addition, the second case study is used to compare the different observational methods determining evapotranspiration (Sect. 3.3) with each other. Because of the nearly cloudfree conditions, model runs with assimilation of radiation and rain were not performed for this case, but sensitivity studies with respect to the soil moisture were made. The third case, however, is suitable for both testing the sensitivity of the simulated evaporation and boundary layer structure to the soil moisture, and for assimilation runs.

3.2. Assimilation of radar and satellite data

Precipitation and solar radiation derived from remotely sensed data are assimilated into the SVAT module of the LM to improve the temporal development and spatial distribution of modelled evapotranspiration. The general aspects of the assimilation scheme are shown in Fig. 4. The assimilation of precipitation is based on data of composite images derived from the radars operated by the DWD. These data have a spatial resolution of 4 km and are provided every 15 min. The required rain rates are calculated from radar reflectivity using the relation of Marshall et al. (1954). The derived rain rates are bilinearly interpolated in space to the LM grid and linearly interpolated in time in order to obtain data for each time step of the LM. If necessary, clutter in the radar images is extracted by comparison with METEOSAT data.

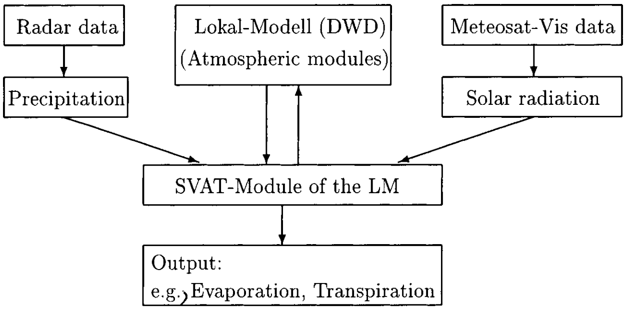

Fig. 4. Scheme for the assimilation of radar-derived precipitation and METEOSAT data into the LM. For explanation see text

The actual solar radiation at the surface is derived from data of the visible channels with wavelengths between 0.4 and 0.9 μm of METEOSAT 5 (case study 1) and METEOSAT 7 (case study 3). These data have a temporal resolution of 30 min and a spatial resolution of approx. 65 km^2 and 20 km^2, respectively, at the geographical position of the considered area (visible data of METEOSAT 5 are only available to us at the resolution of the IR channel for case 1). A simple radiation transfer scheme according to McNider et al. (1995) is used to retrieve cloud reflection, absorbed solar radiation, and for the derivation of shortwave radiation at the ground. This radiation transfer scheme takes Rayleigh scattering by gases and aerosol, molecular absorption, absorption in a cloud layer and reflection at the ground into account making use of empirical formulations. The scheme was slightly modified by using the variable surface albedo implemented in the LM. The derived solar radiation is interpolated in space from the coarse grid of the METEOSAT images to the finer grid of the LM. Radiation fluxes are calculated by the model every 30 min for the same time as METEOSAT images. Therefore, no interpolation in time is necessary here.

Once calculated, precipitation and solar radiation are assimilated into the SVAT module of the LM. Consequently, the solar part of the original radiation transfer scheme and the model predicted precipitation of the LM are switched off for the SVAT module in the assimilation mode. The atmospheric modules of the LM are only influenced by the assimilation through their coupling with the SVAT module.

To test the assimilation scheme, a set of four model runs was performed for case study 1 (in 1994) and case study 3 (in 1998). The first run is a control run without any changes to the model (control run). Model runs with the assimilation of either solar radiation (SR-run) or precipitation (P-run) are made in run two and three, respectively. In the fourth model run both, solar radiation and precipitation, are assimilated (PSR-run).

3.3 Ground-based measurements

Various ground-based measurements were made during summer 1998 to investigate the lower part

Table 1. Soil and vegetation parameters for measurement site "Klein-Altendorf"

Soil Type	Sandy Loam
Tree Height	2.50 m
Leaf Area Index	1.3–1.9
Root Depth	0.60 m

of the atmospheric boundary layer and for the comparison with LM simulations. The field campaign was carried out within a fruit orchard of the "Obstversuchsgut Klein-Altendorf" owned by the University of Bonn. The site is located in a flat area approximately 20 km southwest of Bonn. In this area fruit orchards and tree nurseries with similar sizes of trees and leaf area indices cover an area of around 25 km^2 and are the dominant land use category. The particular site was chosen, because it is representative for large parts of the area and different independent ground-based measurements could be carried out simultaneously. The measurements took place in a field of apple trees (0.2 km^2, for further parameters, see Table 1) which was surrounded by other orchards.

An overview of the different types of measurements and instruments can be found in Table 2. A profile station with instruments at five levels was used to measure the atmospheric conditions up to 6 m above the earth's surface as well as precipitation and soil temperatures continuously from June to September 1998. The instrumentation consisted of 5 psychrometers, 5 anemometers, a windvane, a net radiation sensor, a soil temperature sensor and a raingauge. During several periods from June to September 1998 turbulence measurements were

Table 2. Ground-based measurements 1998

Quantities	Sampling/ Averaging Rate	Heights	Instrumentation	Measurement Periods
Temperature, Humidity	10 s/15 min	2.1 m, 2.9 m, 3.7 m, 4.6 m, 5.7 m	Psychrometers, manufactured at the Meteorological Institute Bonn (MIUB)	June–October
Wind Speed	counts/15 min	2.1 m, 2.9 m, 3.7 m, 4.6 m, 5.7 m	Switching Anemometers, Model A100R, Vector Instruments	
Wind Direction	10 s/15 min	6.2 m	Windvane, Thies	
Net Shortwave Radiation	10 s/15 min	5.1 m	Net Radiation Sensor, Model 8110, Thies	
Soil Temperature	10 s/15 min	−0.02 m, −0.05 m, −0.1 m, −0.2 m, −0.5 m	Soil Temperature Sensor, MIUB	
Precipitation	1 min	1 m	Raingauge, Thies	
Longwave Radiation (upward)	2 s/5 min	1 m, 4.7 m	Pyrgeometers, Eppley	June–October
3D Wind Vector, Temperature	0.1 s/30 min	6 m	Ultrasonic Anemometer, Model USA-1, Metek	17 periods of 1–3 days within June–September
Humidity	0.1 s/30 min	6 m	Infrared Hygrometer, Model M-100, Applied Technologies	15 periods of 1–3 days within June–September
Temperature	0.1 s/30 min	6 m	Platinum Wire Probe, Atmospheric Instrumentation Research (AIR)	5 periods of 1–3 days within June–September
Temperature, Humidity, Wind Speed, Wind Direction	1 min	5 levels (25 m to 200 m)	Tethersonde System, Model TS-5A-SP, AIR	8 June, 13 June, 6–7 August, 18–20 August, 31 August
Tree Transpiration (Sap Flow)	5 s/10 min	–	Sap Flow Meters, manufactured at the Institute for Fruit and Vegetable Production Bonn	June–October

made with a frequency of 10 Hz to get direct measurements of sensible and latent heat flux. The three-dimensional wind vector and temperature were measured by an ultrasonic anemometer and water vapour density was determined by an infrared hygrometer. On several days during the field campaign a tethered balloon with five tethersondes was lifted up to a height of 200 m to get profiles of the lower part of the atmospheric boundary layer.

The energy exchange at the earth's surface is described by the energy balance equation:

$$Q_0 - B_0 - H_0 - E_0 = 0.$$

Q_0 represents the net radiation, which is measured directly by the profile station. B_0 is the soil heat flux, which is calculated from the gradient of the soil temperature and the soil parameters of the soil type of the orchard area. H_0 and E_0 are the turbulent fluxes of sensible heat and latent heat, respectively, between the atmosphere and the surface. Under conditions of horizontal homogeneity these fluxes can be described using the K-theory:

$$H_0 = -\rho_a c_p K_H \frac{\partial \theta}{\partial z}; \qquad E_0 = -\rho_a L K_E \frac{\partial q}{\partial z},$$

with ρ_a the air density, c_p the specific heat capacity at constant pressure, L the latent heat of fusion of water, K_H and K_E the turbulent diffusivities of heat and water vapour, and finally $\frac{\partial \theta}{\partial z}$ and $\frac{\partial q}{\partial z}$ the vertical gradients of the potential temperature and the specific humidity at the measurement level.

Assuming equality of turbulent diffusivities, the turbulent energy fluxes can be calculated by the Bowen ratio energy balance method (Bowen, 1926) by measuring only the gradients of temperature and specific humidity above the considered surface by profile measurements. For the calculation of the energy fluxes presented in Sect. 5 only the four upper psychrometers are taken to avoid the canopy layer of the apple tree stand (see Tables 1 and 2). The turbulence measurements are used to obtain direct measurements of turbulent fluxes applying the eddy covariance technique (Foken and Wichura, 1996; Svensson, 1997).

The latent heat flux calculated directly above the considered field of apple trees represents the total evapotranspiration, which can be divided into transpiration from the apple trees and evapotranspiration from the soil covered with grass between the rows of apple trees. The contribution of tree transpiration was measured using continuous sap flow measurements on eight trees. Here, water flow through the stem was estimated using the heat balance method applied by Sakuratani (1981): a stem section is heated and energy input as well as energy losses are measured. The remainder between input and losses is the energy conducted away with the xylem sap. As the increase in sap temperature is measured as well, absolute mass flow can be calculated accordingly. A detailed description can be found in Weibel and Vos (1994) while modifications are described by Braun and Schmid (1999). The time resolution was 10 min, but data were averaged over 30 min for comparison with turbulence and Bowen ratio measurements. Leaf area of each tree was determined and data were then calculated on a per unit leaf area basis rather than on a per tree basis. This eliminated differences in transpiration between trees and allowed for a spatial upscaling of results to the whole orchard area by multiplying with the leaf area index. Transpiration data have been converted to energy flux units.

4. Assimilation results

4.1. Strong rain event (case study 1)

The first simulation represents a case with strong rainfall associated with a squall-line (4 July 1994) as outlined in Sect. 3.1. A more detailed description of the general weather situation can be found in Drüen and Heinemann (1998). For this case, simulated precipitation and solar radiation in the control run differ considerably from the measured quantities derived from radar and METEOSAT data. Early in the morning the sky was clear, and around 9 UTC first clouds were observed in the NRB. At 12 UTC most of the area was covered by a large compact cloud cluster as can be seen in the METEOSAT VIS image (Fig. 5b). This cloud cluster crossed the area and moved eastwards later on. Details of the precipitation event and additional satellite and radar imagery are shown in Reudenbach et al. (this issue). In contrast to the METEOSAT VIS measurements, simulated cloudiness (without assimilation, Fig. 5a) essentially does not change during the day although the model predicts the cold front. For the

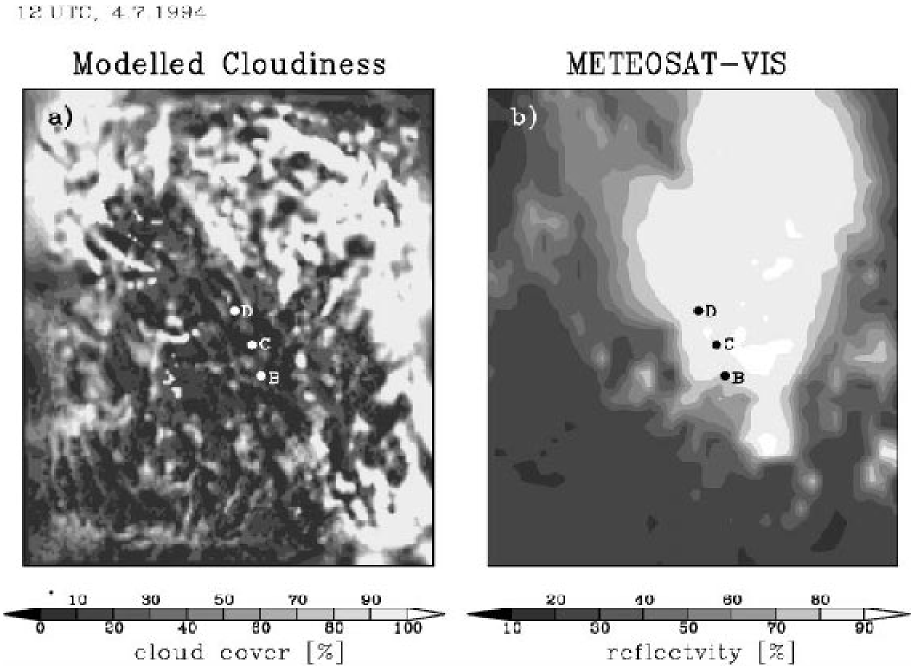

Fig. 5a. Cloudiness for 4 July 1994 at 12 UTC for the LM model area simulated by the LM, and **b** reflectivities given by the METEOSAT VIS data for the same area. Light areas belong to cloudy parts, dark ones to cloud free parts. If the reflectivity exceeds 30% we assume existence of clouds. Points D, C, and B indicate the location of the cities Düsseldorf, Cologne and Bonn, respectively

whole day, modelled clouds have a patchy structure as shown for 12 UTC in Fig. 5a.

Around 9 UTC it started to rain in some parts of the NRB area reaching NRB area mean rain rates of up to 6 mm h^{-1} around 11 UTC. In contrast, simulated rain rates reach only NRB area mean values of up to 2 mm h^{-1}. The differences between measured and simulated cloudiness and precipitation have of course large influences on development, spatial pattern and amount of modelled evapotranspiration.

All four model runs (Sect. 3.2) started at 0 UTC, 4 July 1994, while the assimilation of precipitation and solar radiation started in the morning at 9 and 7 UTC, respectively.

Figure 6 shows the spatial distribution of latent heat flux for 4 July 1994 for the four different model runs at 12 UTC. The pattern of the control run (Fig. 6a) is characterized by many local spots with very high values of latent heat flux. This pattern is produced by local precipitation and local cloudiness generated by the LM. These spots disappear when both, precipitation and solar radiation, are assimilated (PSR-run, Fig. 6d), because the measured precipitation is spatially more continuous. Furthermore, temporal development and spatial extension of radar-derived precipitation agrees well with the METEOSAT images. As expected, the pattern of latent heat flux of the SR- and PSR-run (Fig. 6b, d) resembles the cloud cover shown in Fig. 5b. The assimilation of solar radiation reduces the latent heat flux in some areas strongly. But in contrast to the SR-run, this reduction is weakened in the PSR-run, since measured rain rates are higher and spatially more continuous. The assimilation of radar-derived rain rates results in a more continuous distribution of latent heat flux (Fig. 6c). But for large areas, the obtained latent heat flux reaches unrealistically high values, because rain rates are assimilated also in areas of high solar radiation due to the few simulated clouds (Fig. 5a). The pattern of the SR-run still contains the local spots with extremely high values of latent heat flux, because here measured cloudiness is combined with simulated precipitation. In comparison to the control run (Fig. 6a), the assimilation of both parameters (Fig. 6d) changes the spatial distribution of latent heat flux considerably to realistic values.

Figure 7 shows the temporal development of solar radiation at the surface, precipitation and evapotranspiration for the four simulations as area mean values for the subarea NRB (Fig. 2). Solar radiation and evapotranspiration of the control run show a typical diurnal cycle for a day with constant cloud cover. In contrast to the modelled solar radiation, solar radiation derived from METEOSAT data is influenced by the large compact cloud layer crossing the area during the day. The evapotranspiration of the SR- and PSR-

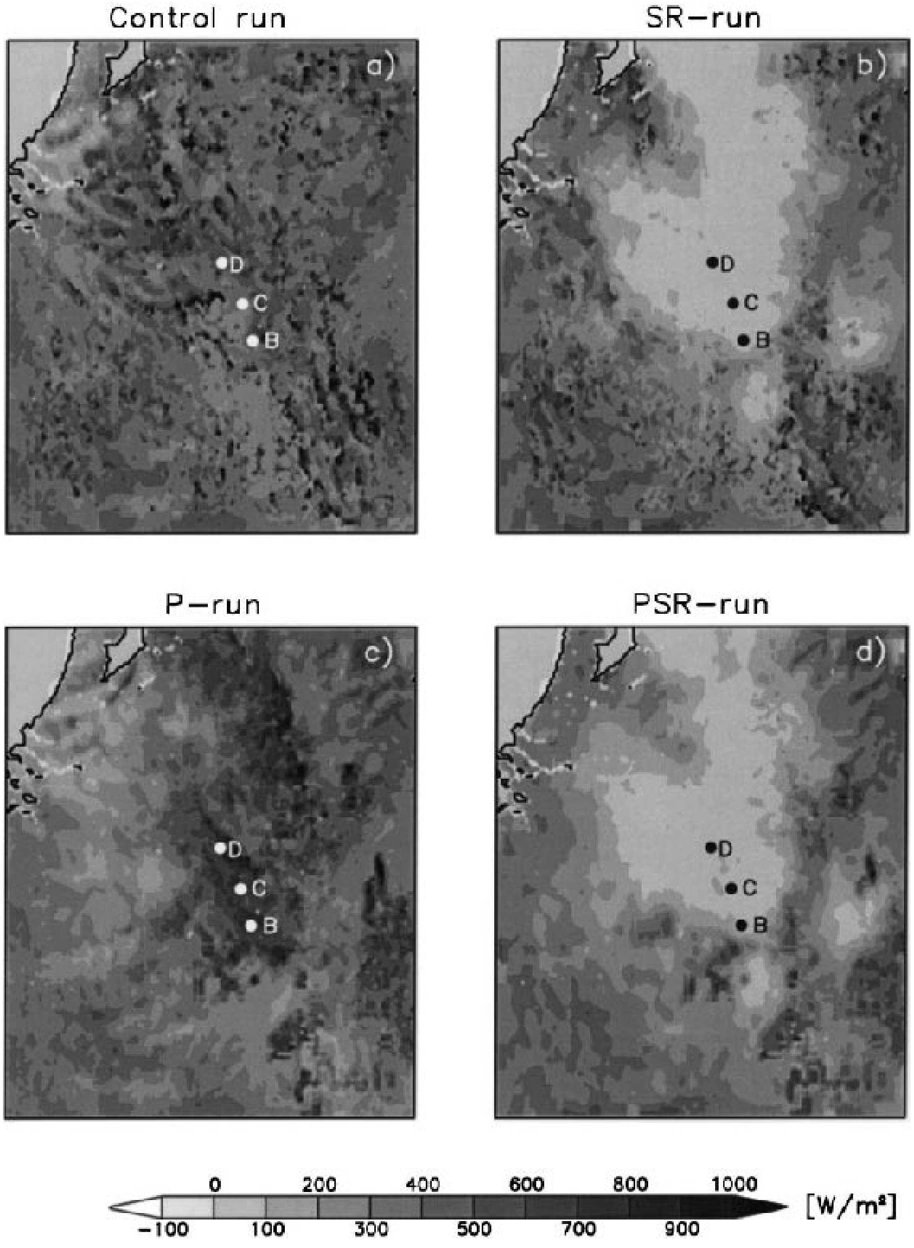

Fig. 6. Simulated latent heat flux for 4 July 1994 at 12 UTC for the LM-model area, **a** without any modifications (control run), **b** with the assimilation of solar radiation (SR-run), **c** with the assimilation of precipitation (P-run), and **d** with both assimilation of solar radiation and precipitation (PSR-run). Points D, C, and B indicate the location of the cities Düsseldorf, Cologne and Bonn, respectively

run follows the course of the METEOSAT-derived solar radiation. In the morning, the difference between these runs and the control run is small due to the rather low soil moisture, but with increasing cloud cover evapotranspiration of the assimilation model runs is strongly decreased. Mean radar-derived precipitation has most of the time higher values than the modelled one, and maxima are reached at different times. Therefore, and since there are only few modelled clouds, evapotranspiration in the P-run reaches higher values around noon. Using both assimilations simultaneously (PSR-run), the tendencies of the SR- and the P-run are combined in the way that extremes of each run are weakened.

The assimilation of radar-derived precipitation does neither influence the model's vertical precipitation structure nor the structure of the dynamical fields to a large extent in this case. Since the assimilation affects only the surface energy and hydrological balance, all changes compared to the control run must be transported through the boundary layer. This is not the case for the SR- and PSR-run. The model produces less rain ($1\,\mathrm{mm\,h^{-1}}$) when assimilating shortwave radiation, regardless of the precipitation assimilation. A

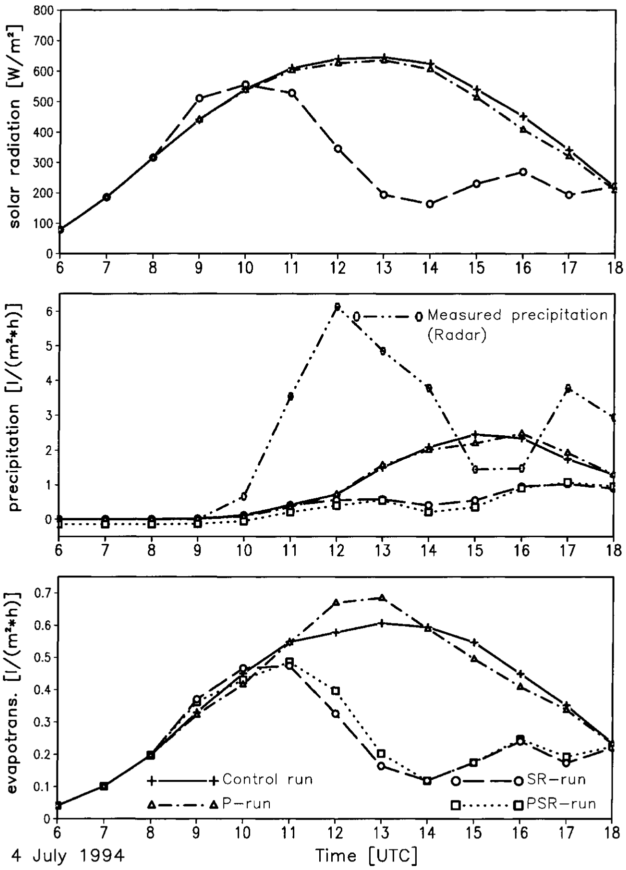

Fig. 7. Temporal development of NRB area mean values of solar radiation, and precipitation evapotranspiration for 4 July 1994. The different model runs are without and with assimilations of solar radiation and precipitation (control, P-, SR- and PSR-run). The PSR-run is not shown for solar radiation, because it is equal to the SR-run

possible reason could be that the decrease in solar radiation around 9 UTC comes along with a reduction of convective instability compared with the control run. Therefore the convective activity is weaker compared to the control run during the passage of the front and only a minor peak in the precipitation rate occurs. A second rain event in the late afternoon is indicated in the SR- and PSR-run, while in the other model runs only one event is simulated. This peak corresponds with an additional second rainfall maximum in the radar-derived precipitation, but the simulated precipitation does not reach the observed values by far. Nevertheless, the improvement of the assimilation for the surface energy and hydrological balance is obvious compared to the control run.

Of extreme importance for hydrological applications, e.g. runoff calculations, are the amounts of evapotranspiration and precipitation integrated over a precipitation event. For the control- and PSR-run the sum of evapotranspiration for 18 hours is 5.3 mm and 3.4 mm, respectively, compared to the sum of precipitation of 13 mm and 28 mm, respectively.

4.2. High-pressure summertime weather situation for Central Europe-case study 3

The impact of assimilation on evapotranspiration was also studied for the period of 19 to 21 August 1998. As outlined in Sect. 3.1, the 19 August and the morning of 20 August were mostly sunny. In the afternoon of 20 August, more clouds developed and in the night of 20 to 21 August a front crossed the area developing some rain showers (NRB area mean values of 1 mm h^{-1}). On 21 August, it rained most of the time in connection with a second front that crossed the area (area mean values of up to 3 mm h^{-1}). In general, the model simulates the development of both fronts. Nevertheless, there are some differences between simulated precipitation and solar radiation and measured parameters. This causes differences in the temporal development and the spatial distribution of evapotranspiration.

Again, four model runs were made (Sect. 3.2). All model runs started at 0 UTC of 19 August 1998. In the following, results of 20 and 21 August are described in more detail. The results for 19 August are very similar to the ones obtained for 20 August.

In general, for 20 August solar radiation in all model runs exhibits a typical diurnal cycle for a mostly sunny day (Fig. 8). However, in the morning the simulated solar radiation remains below assimilated values. This is due to high clouds in the whole area in the control run during the day (Fig. 9a), which reduce the modelled solar radiation at ground. Consequently, in the morning the evapotranspiration in the SR- and PSR-run reaches slightly higher values than in the control run. In the afternoon, the assimilated solar radiation is reduced by developing clouds in contrast to the control run. In the night, the model also develops thicker clouds, which reduce the energy losses due to the net radiation to about −30 W m^{-2} during the night (not shown). Around 20 UTC on the 20 August the radar data show the beginning of a rain event while the model does

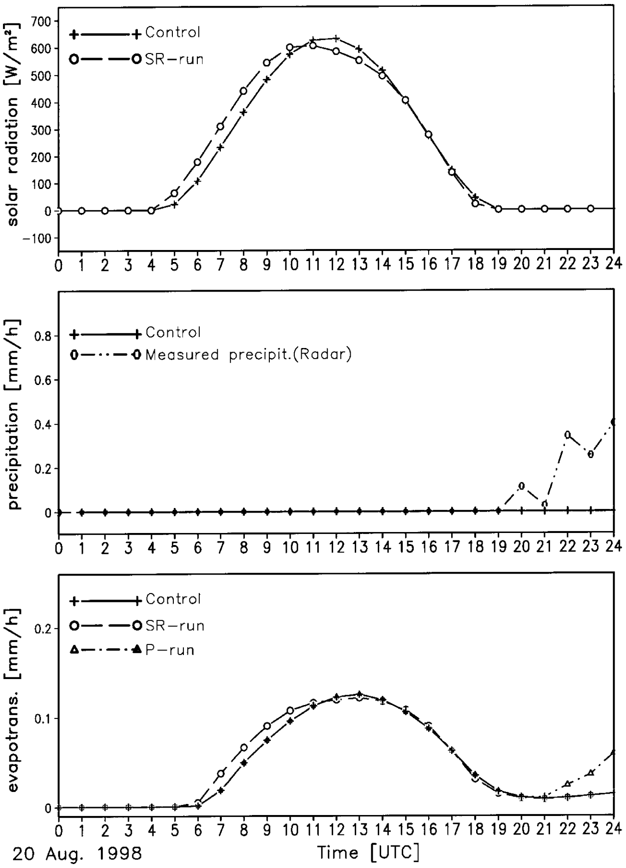

Fig. 8. As Fig. 7, but for 20 August 1998. PSR-run is omitted, because its similarity to the SR run due to the lack of precipitation

not simulate precipitation. The combination of modelled thick cloudiness and assimilated precipitation causes higher amounts of evapotranspiration during the night of 20 to 21 August in the P- and PSR-run in contrast to the control run.

For 21 August, the time lag between the passage of modelled and observed fronts leads to the main differences in the simulated evapotranspiration between the four model runs (Fig. 10). The first front passed in the early morning and the second one in the early afternoon on 21 August, as it is indicated by the main rain events measured by the radar shown in Fig. 10. In contrast, the model simulates the passage of the fronts in the morning and in the late afternoon of 21 August reaching maximum values of simulated precipitation around 9 UTC and 15 UTC. Furthermore, during the passage of the second front measured rain rates are almost three times higher (3 mm h^{-1}) than simulated ones (1 mm h^{-1}).

Additionally, the model simulates a compact cloud layer for the whole day, whereas the METEOSAT VIS images show more structure in the cloud cover and even some cloudfree parts during the day. Consequently, the assimilated solar radiation reached higher values (up to 260 W m^{-2}) compared to the modelled ones in the control run (up to 100 W m^{-2}, Fig. 10). These differences lead to considerably higher amounts of

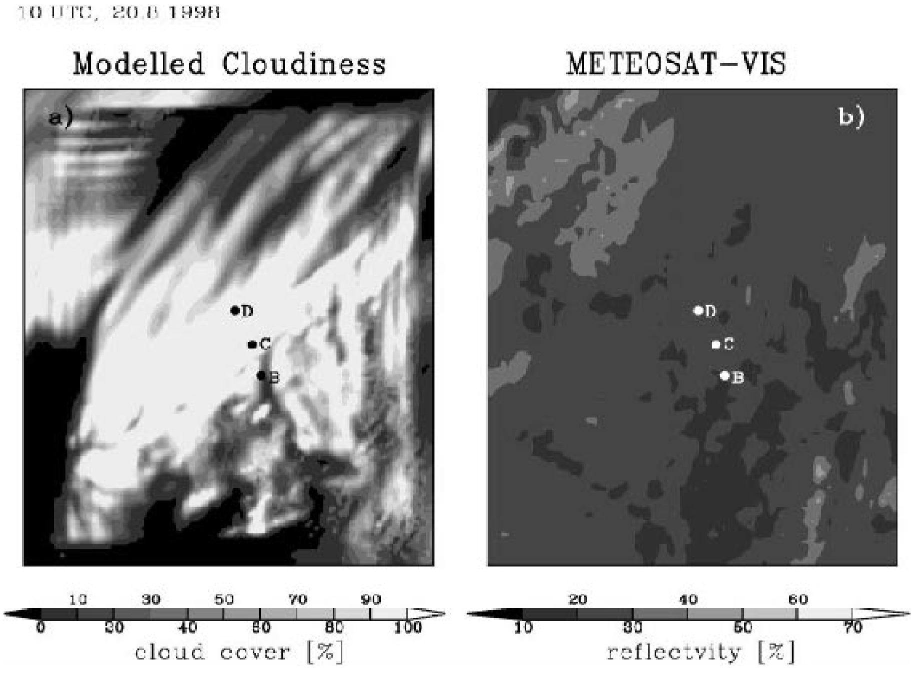

Fig. 9. As Fig. 5, but for 20 August 1998 at 10 UTC

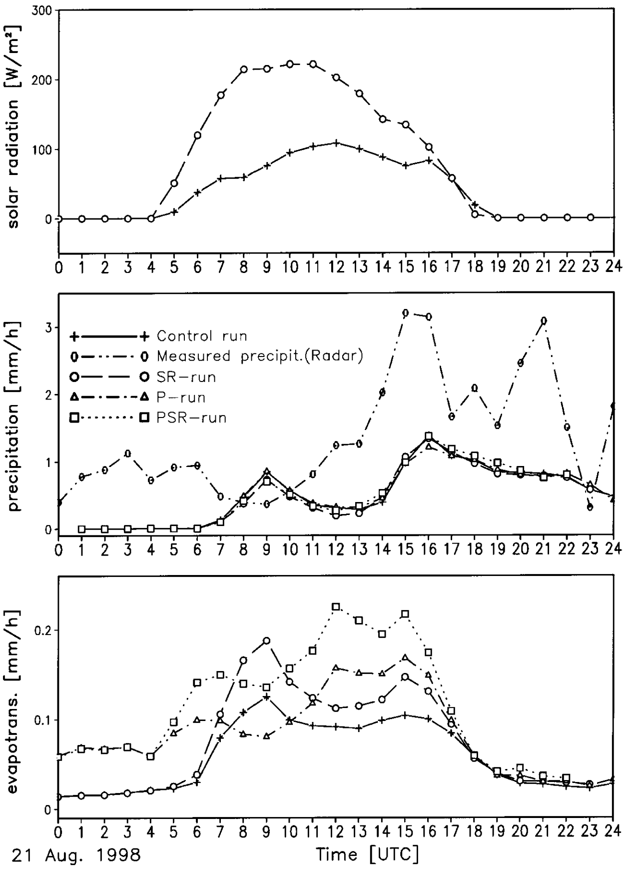

Fig. 10. As Fig. 7, but for 21 August 1998

evapotranspiration for the SR- and PSR-run and different temporal development for the P- and PSR-run in contrast to the control run.

In general, the assimilation of precipitation as well as of solar radiation causes largely different spatial distributions of evapotranspiration in comparison to the control run. This is exemplarily shown in Fig. 11a and b, where the spatial distribution of latent heat flux for the whole LM area is plotted for 12 UTC on 21 August. However, although the amount of evapotranspiration of the PSR-run is higher compared to the control run, it is still too low compared to measurements (see Sect. 5), which is likely a result of the low initial soil moisture content of the model.

5. Comparison with ground-based measurements

The model simulations of surface layer quantities, surface energy balance components, and boundary-layer structures can be compared with measurements for case studies 2 and 3 (we have no measurements for case study 1 in 1994). The intercomparison of different measuring methods (shown below) yields a good agreement with respect to the sensible and latent heat fluxes, but large discrepancies are found for the comparison with the simulated fluxes. Since soil moisture is a

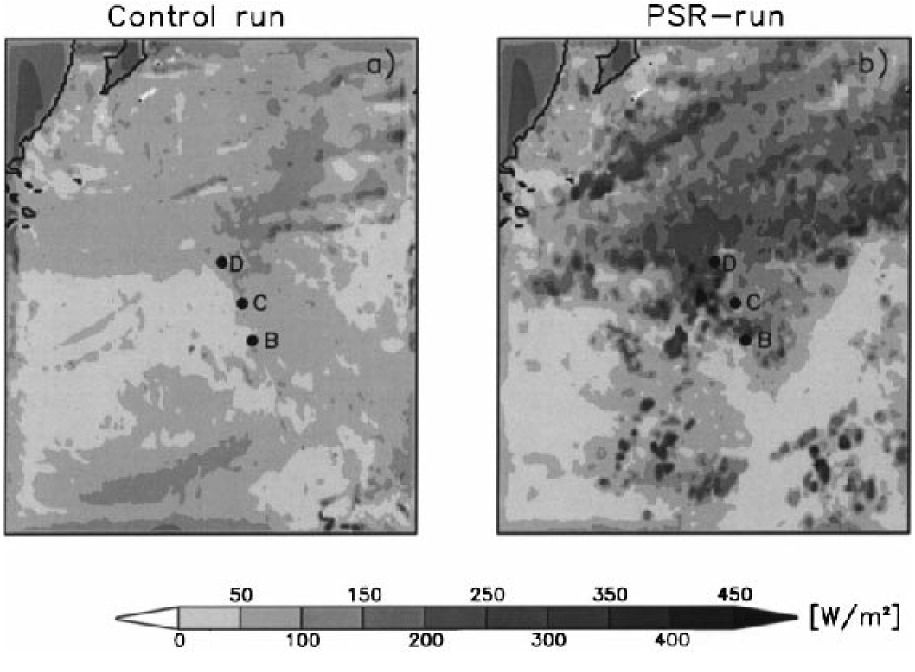

Fig. 11. As Fig. 6, but for 21 August 1998 at 12 UTC; **a** control run, and **b** PSR-run

Table 3. Soil and vegetation parameters for LM grid point "Klein-Altendorf"

Soil Type	Loam
Roughness Length	0.17 m
Plant Coverage	89%
Root Depth	0.68 m

good candidate for the explanation of these discrepancies, sensitivity studies with respect to soil moisture have been performed. A comparison with LM results has been made for case study 2 (6/7 August 1998) using a) the original soil moisture content by the model (SM_{orig} run) and b) assuming a 50% increased soil moisture content (SM+50 run).

For case study 3, four different LM runs were performed for comparison:

a) without any changes to the model (control run);
b) with assimilation of shortwave radiation and precipitation (PSR-run, see Sect. 3.2);
c) assuming a 100% increased soil moisture content (control+100 run), and finally
d) with assimilation and 100% increased soil moisture content (PSR+100 run).

The parameters of the soil and the vegetation for the LM grid point nearest to the measurement site "Klein-Altendorf" are shown in Table 3. They are in good agreement with the observed conditions (see Table 1). As mentioned in Sect. 3.3, these conditions of the measurement site are representative for an area of about 25 km^2.

5.1. Case study 2 – 6/7 August 1998

In Fig. 12 measured near-surface quantities (15 min means) are presented for 6 and 7 August 1998. Temperature, net radiation, wind speed and wind direction are shown for a height of 2 m above the tree tops. Corresponding to the high-pressure conditions during this case study (see Sect. 3.1), the air temperature shows a diurnal variation from about 10 °C in the early morning hours up to 27 °C in the afternoon of 6 August. The strong decrease of air temperature in the evening is combined with an increase of relative humidity just after sunset with dew development (not shown). The wind direction shows a veering of the wind from easterly to westerly directions at about 8 UTC on 6 August, which is accompanied by an increase in the horizontal wind speed (from 1 to 3 m s^{-1}). This increase is connected with the development of a mixed boundary layer during the day. The transition to a stable boundary layer at night is associated with a decrease in wind speed at 18 UTC (from 3 to 1 m s^{-1}) and a backing from westerly to easterly directions.

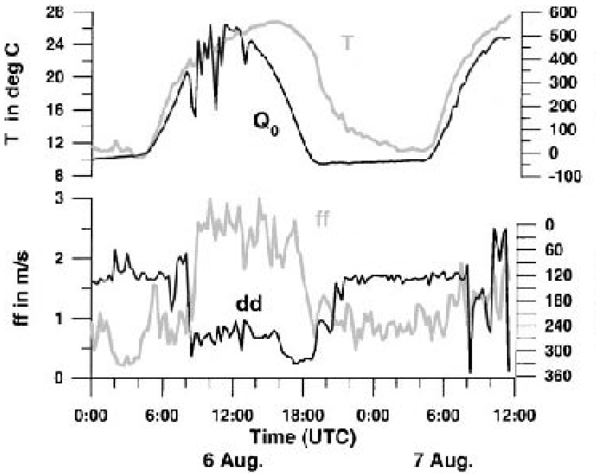

Fig. 12. Measurements of temperature *T*, net radiation Q_0, horizontal wind speed *ff*, and wind direction *dd* (15 min average values) for 6 and 7 August 1998 at Klein-Altendorf (see Fig. 2). Measurement heights are about 2 m above the trees (see Table 1)

Figure 13 shows energy fluxes (30 min means) above the canopy layer of the apple tree stand

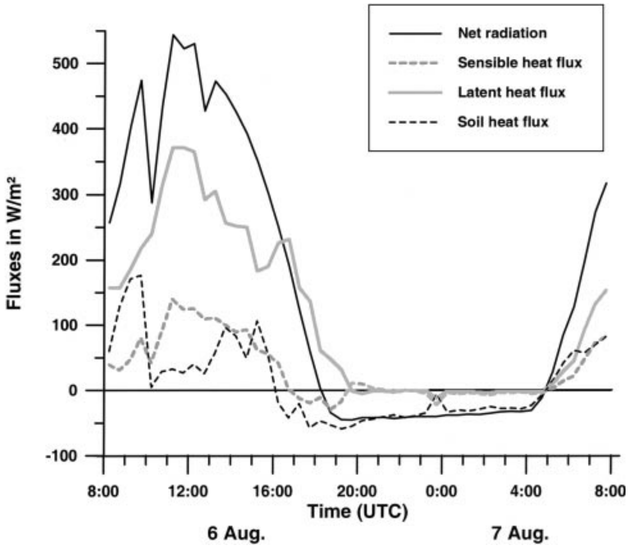

Fig. 13. Components of the surface energy balance for 6 and 7 August 1998 (30 min average values) calculated from profile measurements at Klein-Altendorf by the Bowen ratio method

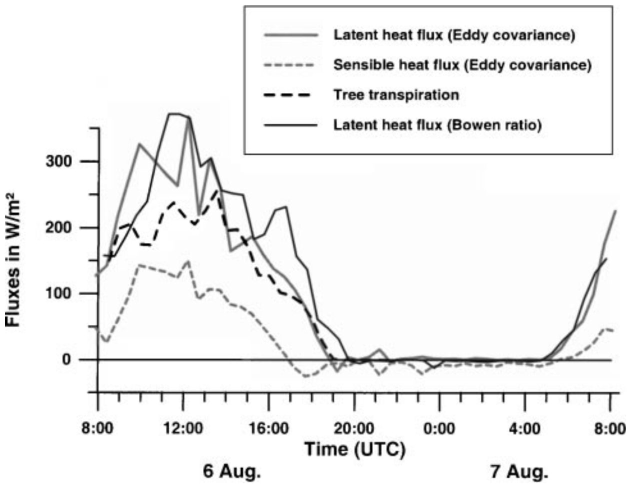

Fig. 14. Turbulent energy fluxes for 6 and 7 August 1998 (30 min average values) calculated from turbulence measurements (eddy covariance technique), the Bowen ratio method, and sap flow measurements

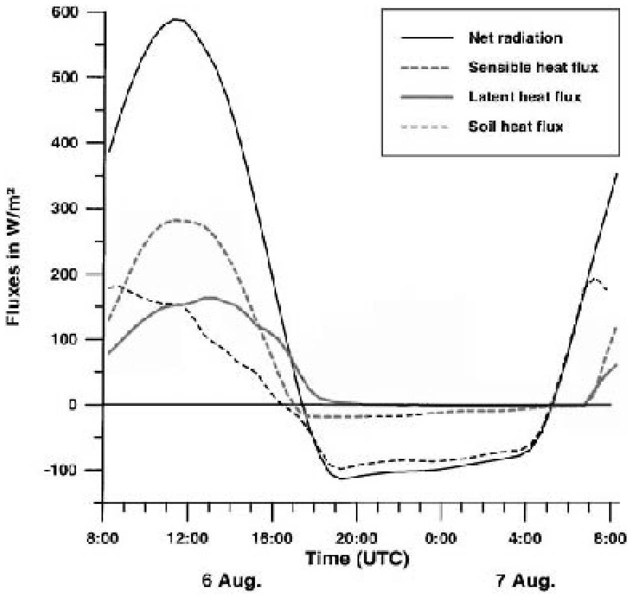

Fig. 15. Components of the surface energy balance for 6 and 7 August 1998 calculated from LM for the SM_{orig} run

calculated by the Bowen ratio energy balance method for 6 August 8 UTC to 7 August 8 UTC. The net radiation exhibits fluctuations in the morning hours due to some clouds at that time. Turbulent heat flux values reach up to 150 W m^{-2} for sensible and up to 350 W m^{-2} for latent heat flux. There is a strong decrease in the Bowen ratio in the afternoon at about 1630 UTC, when the sensible heat flux decreases to almost zero but the latent heat flux is still high due to continuing evapotranspiration at that time.

These results agree well with the direct flux measurements by eddy covariance technique from the turbulence sensors shown in Fig. 14. These calculations show a very similar daily cycle of turbulent fluxes. Maximum values of E_0 and H_0 as well as the diurnal courses agree with Bowen ratio calculations. The strong evapotranspiration in the late afternoon and the weak sensible heat flux can also be recognized from these measurements. The overestimation of the Bowen ratio latent heat flux in the afternoon (E_0 is even larger than the net radiation, see Fig. 13) results from an overestimated negative soil heat flux due to changing shading conditions for the location of the soil temperature sensor. But also the eddy covariance latent heat flux exceeds the net radiation just before sunset. In Fig. 14 the diurnal course of the contribution of tree transpiration from sap flow measurements to the total evapotranspiration is shown additionally. It reaches values below or comparable to the latent heat flux during the day. From 9 UTC to 14 UTC the tree transpiration is accompanied by evaporation from the soil (which can be assumed to be negligible for the very dry topsoil) and by transpiration from the grass between the tree rows. Later in the afternoon it can be noted that nearly all of the latent heat flux can be attributed to tree transpiration.

Energy fluxes calculated from the control run of the LM for the grid point being closest to the measurement site are shown in Fig. 15. Compared to measured energy fluxes in Figs. 13 and 14 the net radiation is simulated quite well during the daytime, but turbulent heat fluxes do not agree. The simulated sensible heat flux reaches almost 300 W m^{-2} while the latent heat flux reaches values of only 150 W m^{-2}. The modelled Bowen ratio at noon is about 2 being in contrast with the measurements showing values of about 0.5. A reason is probably the low soil moisture content in the model for this day. In Fig. 16 the model run with the artificially increased soil moisture content (SM+50 run) is shown. Both, sensible and latent heat flux still do not reach measured values, but the Bowen ratio is now more realistic. During the night, the model predicts much lower values for net radiation compared to the actually measured ones. This is associated with simulated near-surface temperatures being to high (see below).

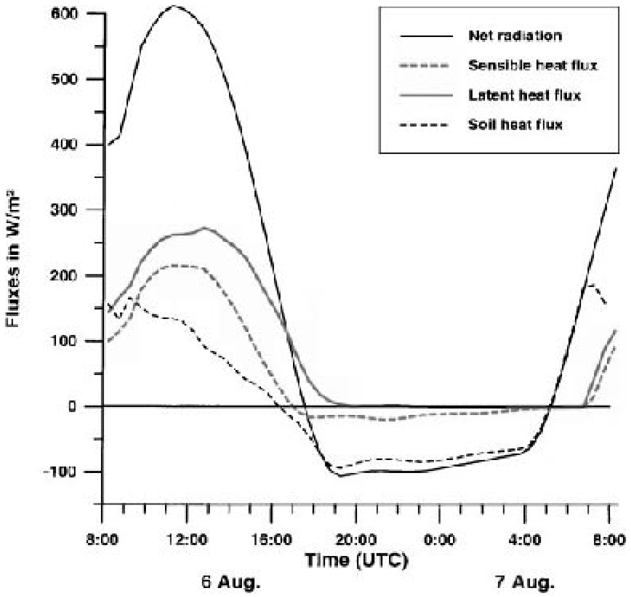

Fig. 16. As Fig. 15, but for the SM+50 run

Table 4. Total amount of evapotranspiration for daytime on 6, 19, and 20 August

	6 August 8–20 UTC	
Bowen Ratio	3.60 mm	
Eddy Covariance	3.78 mm	
Transpiration	2.49 mm	
SM_{orig} run	1.76 mm	
SM+50 run	2.90 mm	
	19 August 6–18 UTC	20 August 6–18 UTC
Bowen Ratio	3.21 mm	3.73 mm
Control run	0.51 mm	0.62 mm
PSR-run	0.48 mm	0.72 mm
Control+100 run	3.51 mm	3.71 mm
PSR+100 run	3.37 mm	4.40 mm

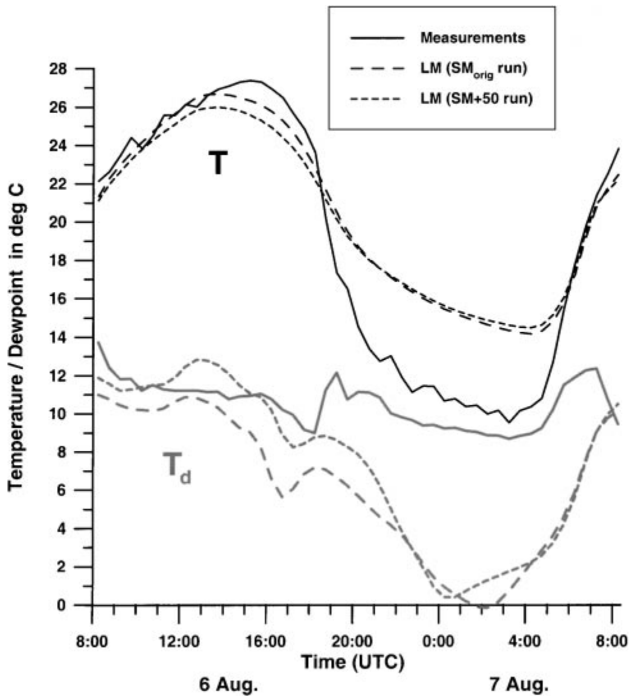

Fig. 17. Measurements of the 2 m temperature and dewpoint for 6 and 7 August 1998 at Klein-Altendorf and from the SM_{orig} and SM+50 runs

The total amount of evapotranspiration for 6 August by integrating the latent heat flux from 8 UTC to 20 UTC is 3.6 mm from the Bowen ratio calculations (see Table 4). As mentioned before, the modelled values for the same period agree quite well for the SM+50 run, but the SM_{orig} run simulates much less evapotranspiration.

In Fig. 17 daily cycles of measured and calculated 2 m temperature and dewpoint are presented. During daytime, model results are comparable to the measurements although there is a time lag of about 3 hours between model and measurements concerning the maximum temperatures. But during the night, the simulated 2 m temperatures are up to 5 °C higher than the measured ones. This results in a too low net radiation at night in both model runs (Fig. 15 and 16) compared to the measured net radiation (Fig. 13). For the dewpoint (Fig. 17) a good agreement between the model run with increased soil moisture content and measurements can be observed for the daytime, but at night the model simulates the near-surface air being too dry independent of the choice of soil moisture content. An intercomparison of boundary-layer structures measured by the tethered sonde system and simulated by the LM yields good agreement except for the stable boundary layer at night (not shown). These results are very similar to those of the third case study (see Sect. 5.2), where the intercomparison is discussed in detail.

5.2. Case study 3 – 19 to 21 August 1998

While for the measurement period presented in the previous section assimilation runs have not been carried out due to the absence of clouds and

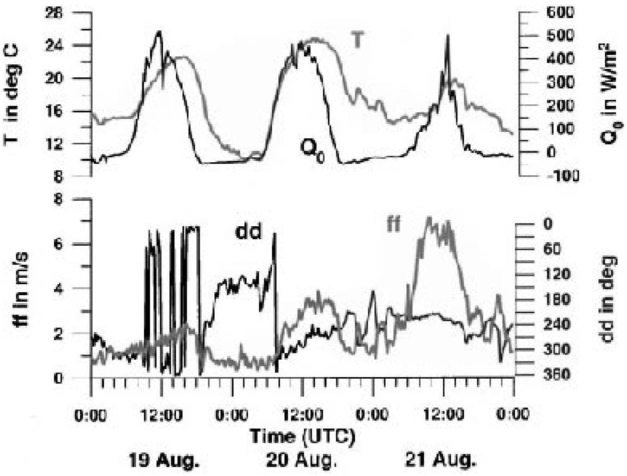

Fig. 18. As Fig. 12, but for 19, 20, and 21 August 1998

rain, four LM runs including assimilation can be compared to measurements for this case study.

Figure 18 gives an overview over the time period between 19 and 21 August 1998. During the first two days fair weather conditions with few clouds prevailed. Values of more than 500 W m^{-2} were measured for the net radiation Q_0. The daily cycle of the temperature shows maximum temperatures of 23 °C and 25 °C, respectively, and minimum temperatures in the early morning down to 10 °C on 20 August. The horizontal wind speed was weak with values between 1 and 3 m s^{-1} during these first two days with northwesterly directions at daytime and southerly directions during the night. On 21 August complete different weather conditions prevailed. In the lower part of Fig. 19 raingauge data is shown (15 min accumulated rain). Showers occurred in the early morning and the afternoon, and later on a rainy period in the evening led to a total amount of 10.8 mm rain for the whole day. The horizontal wind was westerly and showed an increase in wind speed during daytime up to maximum values of 7 m s^{-1} (Fig. 18), which was connected with the passage of the second cold front during this case study (see Sect. 3.1).

Figure 19 shows 30 min average values of the energy fluxes calculated by Bowen ratio energy balance method from the profile measurements. During the whole period the latent heat flux is predominant at daytime compared to the sensible heat flux and the soil heat flux. On the first two very sunny days the latent heat flux increases up to 350 W m^{-2}, the sensible heat flux and the soil heat flux reach values of 150 W m^{-2} only. On the third day the latent heat flux gets even more predominant than the days before. Especially in the morning hours (after the first rain event) it is slightly higher than the net radiation because of still negative values of the sensible and soil heat fluxes. At nighttime negative values of the net radiation go down to -50 W m^{-2} during the first two nights with clear sky conditions. This energy loss is compensated by a strong soil heat flux directed from the deeper soil to the surface with values of -50 to -70 W m^{-2}.

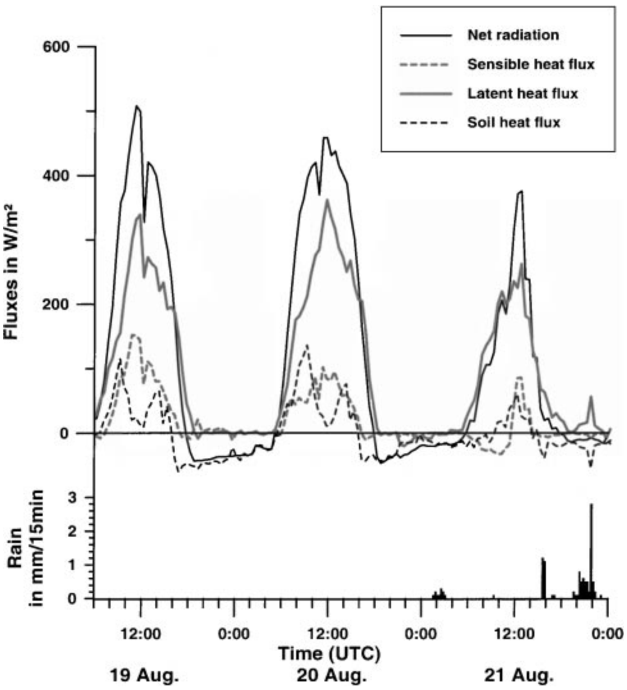

Fig. 19. As Fig. 13, but for 19, 20, and 21 August 1998. In addition, rainfall measured by a rain gauge is shown as 15 min accumulations

Four model runs were performed with the LM, a control run, a PSR-run, and two further model runs (control+100 run and PSR+100 run) where soil moisture was artificially increased by 100%. An increase of the soil moisture content by only 50% leads to no significant changes. The energy fluxes of these four runs and the interception of precipitation in the model (30 min accumulations) are presented in Fig. 20 (control run), Fig. 21 (PSR-run), Fig. 22 (control+100 run), and Fig. 23 (PSR+100 run), respectively. The results of the control run are qualitatively similar to the first-case study. The net radiation is simulated quite well for the first two days, but the sensible heat flux is much too large and the latent heat flux

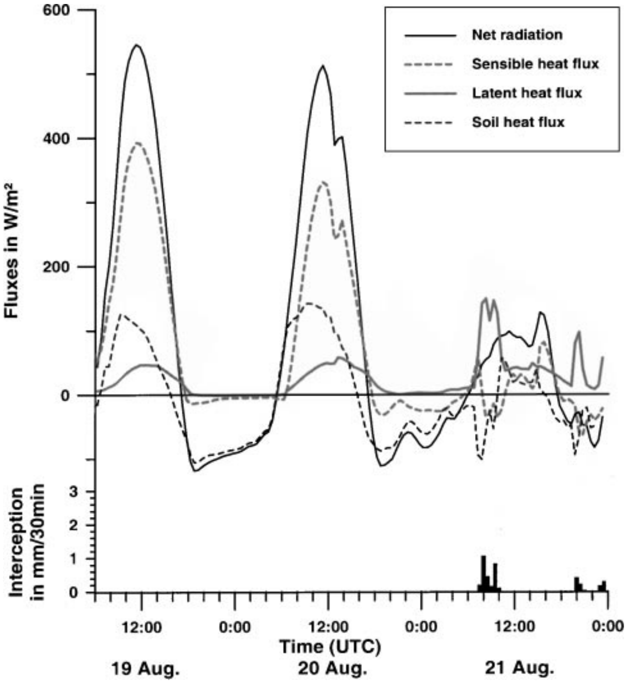

Fig. 20. As Fig. 15, but for 19, 20, and 21 August 1998 for the control run. In addition the interception storage of precipitation (simulated by the LM) is shown as 30 min accumulations

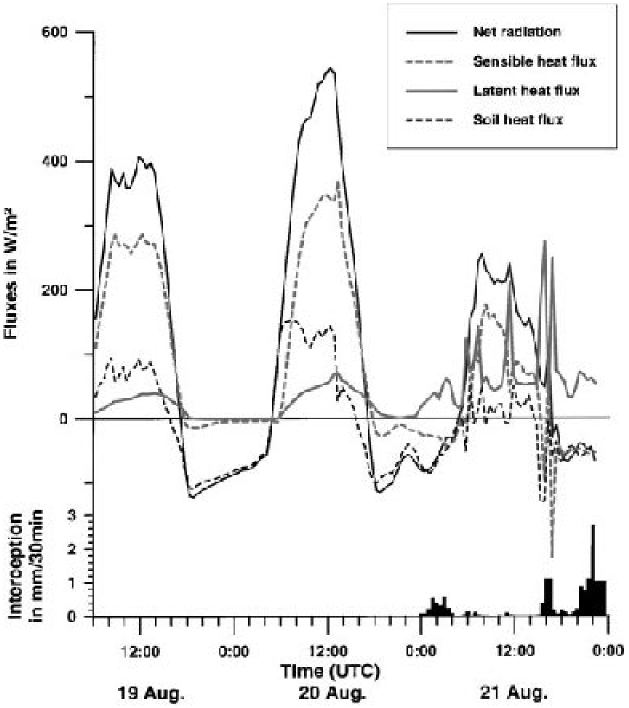

Fig. 21. As Fig. 20, but for the PSR-run (using radar-derived rain)

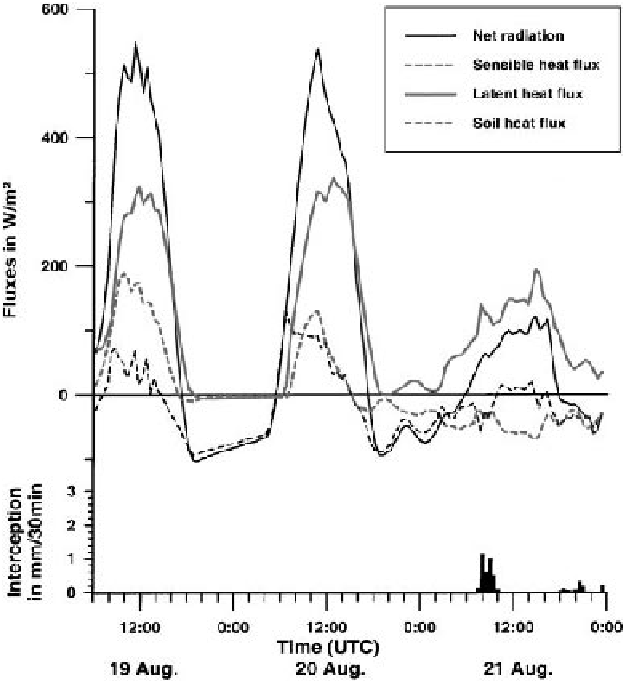

Fig. 22. As Fig. 20, but for the control+100 run

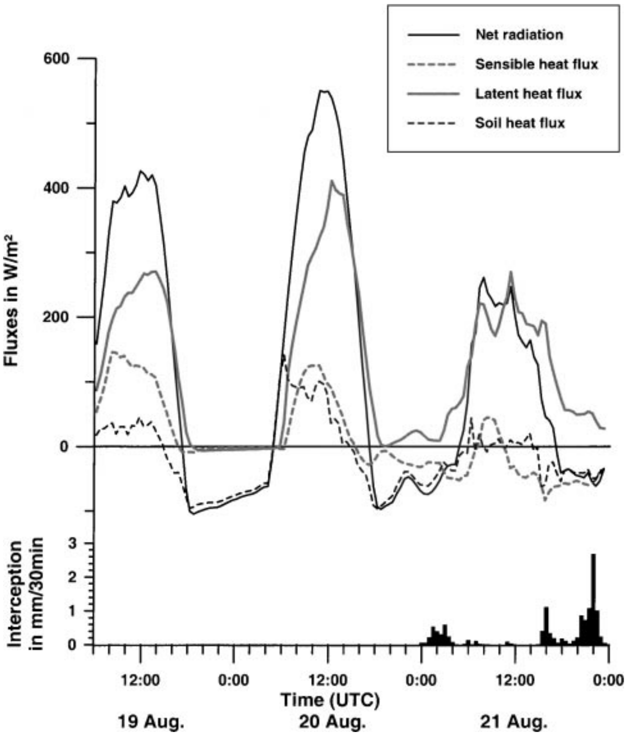

Fig. 23. As Fig. 21, but for the PSR+100 run

much too low. On the third day with rain in the early morning and the evening, the simulation gets better with respect to the Bowen ratio, but the net radiation and the latent heat flux are simulated much too low during daytime. The rain events on 21 August are also modelled quite badly. The first event in the early morning is not simulated at all, and the rainy period in the evening is much too weak compared to the measurements.

The assimilation of solar radiation and radar-derived precipitation (PSR-run, Fig. 21) causes changes for the surface fluxes and the interception storage of precipitation, which is controlled directly by the radar-derived rain entering the SVAT-module. Compared to the control run, the net radiation is simulated better on the third day but worse on the first day. This modification however does not result in a change of the ratio of sensible and latent heat flux on the first two days. The comparison to the measurements (Fig. 19) shows that the rain events on 21 August are represented very well in this run giving some confidence in the radar-derived rainfall estimates used for input. This results in an increase of the soil moisture content in the first soil layer in the evening of 21 August (not shown) comparable to the soil moisture in the runs with artificially increased soil water content. Thus the assimilation effects should be visible not before the following day in this run.

The simulation results for the turbulent surface fluxes improve for the whole period by increasing the soil moisture in the last two model runs (Figs. 22 and 23). The sensible and latent heat fluxes now agree well with the measurements (Fig. 19). Some clouds are simulated during the first two days which agrees with the observations and leads to a reduction of the net radiation during daytime. The assimilation of satellite-observed shortwave radiation and precipitation into the model with increased soil moisture shows improvements especially on the third day, but the simulation of the surface fluxes for the first two days is still worse compared to Fig. 22. In both assimilation runs (see Figs. 21 and 23) the net radiation is overestimated during daytime on 20 August. The used solar radiation assimilation scheme (McNider et al., 1995) reduces the amount of simulated cloudiness, especially if there are only few clouds. This leads to an overestimation of short-wave radiation fluxes and to a too high net radiation during the day. Thus, the transmittivity of the atmosphere used in the assimilation scheme seems to be much higher compared to both reality and the control runs. This is one of the disadvantages of the applied assimilation scheme, when almost cloud-free conditions prevail.

The comparison of the values of total evapotranspiration for 19 and 20 August (see Table 4) shows a very good agreement for the model runs with increased soil moisture (control+100 run, PSR+100 run), but, as expected, much worse values for the control run and the PSR-run for both days.

In addition to the near-surface data shown above, measurements of the boundary-layer structure in the lowest 200 m by the tethered sonde system are used for a validation of the simulations. In the following, time-height cross-sections of potential temperature and wind speed interpolated from the profile station and the tethersonde data are compared with results of the four LM runs. The meteorological variables are measured in heights of approximately 2 m, 4 m, 25 m, 50 m, 100 m, 150 m, and 200 m, whereas the model layers are situated in 33.5 m, 109 m and 202 m. Furthermore the LM diagnoses temperature and humidity in 2 m and wind speed in 10 m.

The observed potential temperature cross-section from 19 August 6 UTC to 20 August 12 UTC (Fig. 24a) shows the development of the well-mixed boundary layer during daytime, being associated with an increase in the horizontal wind speed in the afternoon of 19 August (not shown). During the night only weak winds around 2 m s^{-1} are observed. A strong surface inversion develops during the night with potential temperature gradients of about 0.7 K per 10 m up to a height of 100 m. This very strong stable stratification breaks up in the early morning of 20 August connected with a strong increase in the potential temperature near the ground from 12 °C at 6 UTC up to 23 °C around noon in the mixed layer, when wind speeds of up to 7 m s^{-1} are present.

The results of the LM control run are presented in Fig. 24b. A comparison with the experimental results shows a good correspondence for the horizontal wind speed at nighttime but too low wind speeds during the day on 20 August (not shown). The potential temperature agrees very well with the measurements at daytime, but the development of the nighttime surface inversion is

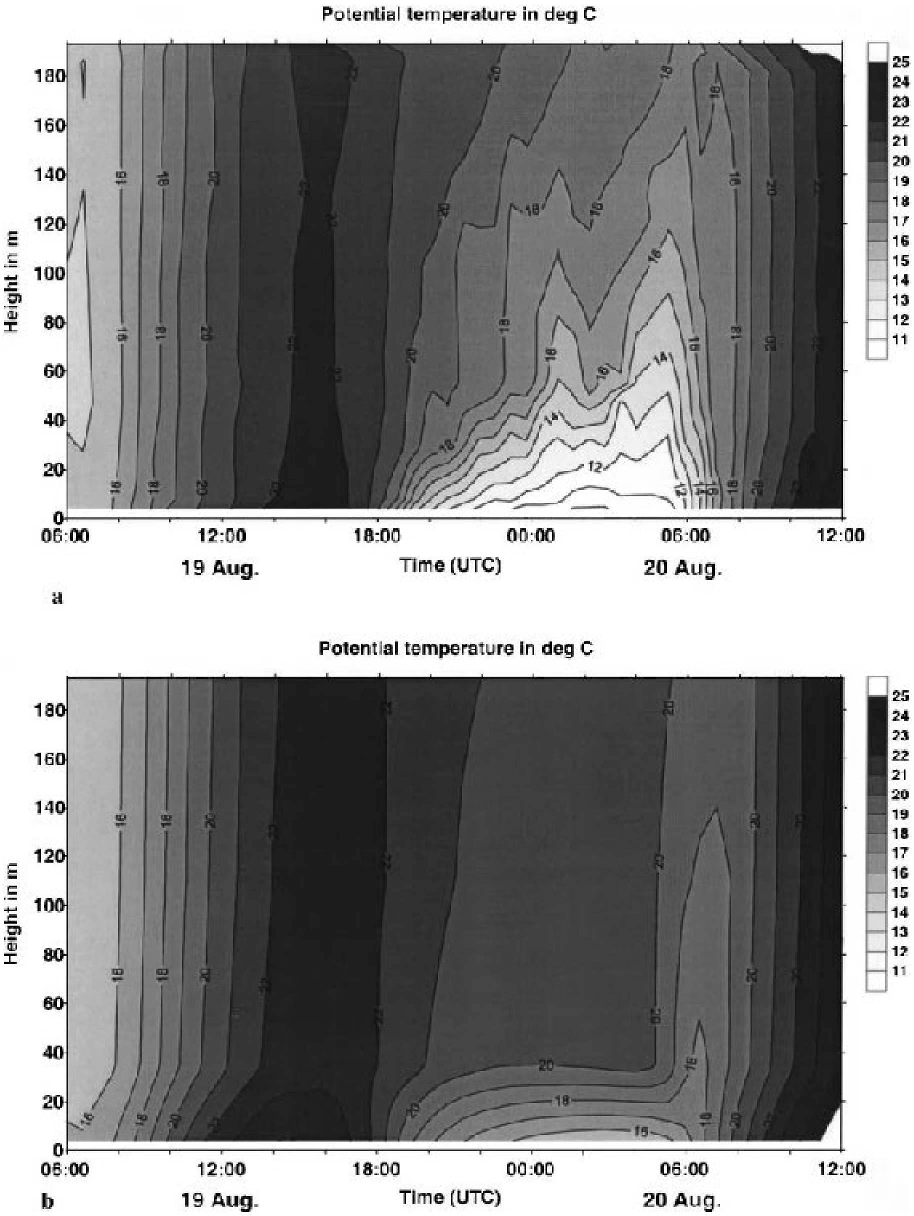

Fig. 24. Time-height cross-sections of potential temperature (isolines every 1 °C) for 19 and 20 August 1998: **a** interpolated from tethersonde data and profile measurements at Klein-Altendorf; **b** for the control run of the LM simulations at the nearest grid point to the measurement site; **c** for the control+100 run, and **d** for the PSR+100 run

not well captured by the model. The underestimation of the vertical extent of the surface inversion is associated with near-surface temperatures being too warm and too low values of the net radiation at the ground in the model (see Fig. 20). In the PSR-run (not shown) there is no significant change in the horizontal wind speed and the potential temperature compared to the control run. The major changes in the PSR-run are an increase of the daytime net radiation and sensible heat flux for 20 August (see Figs. 20 and 21), but the different surface forcing is not strong enough to change the boundary layer structures in the lowest 200 m significantly.

In the last two model runs (control+100 run and PSR+100 run) the cross-sections of the horizontal wind speed are almost the same as in the control run (not shown). But there are significant differences in the cross-sections of the potential temperature (Fig. 24c for control+100 run and d for PSR+100 run). The strong reduction of the Bowen ratio on 19 and 20 August caused by the increase of the latent heat flux (by more than 300 W m^{-2}) and the corresponding decrease in the sensible heat flux (by about 100 W m^{-2}, see Figs. 22 and 23) has a significant effect on the boundary layer structure. Compared to the control run (see Fig. 24b), the

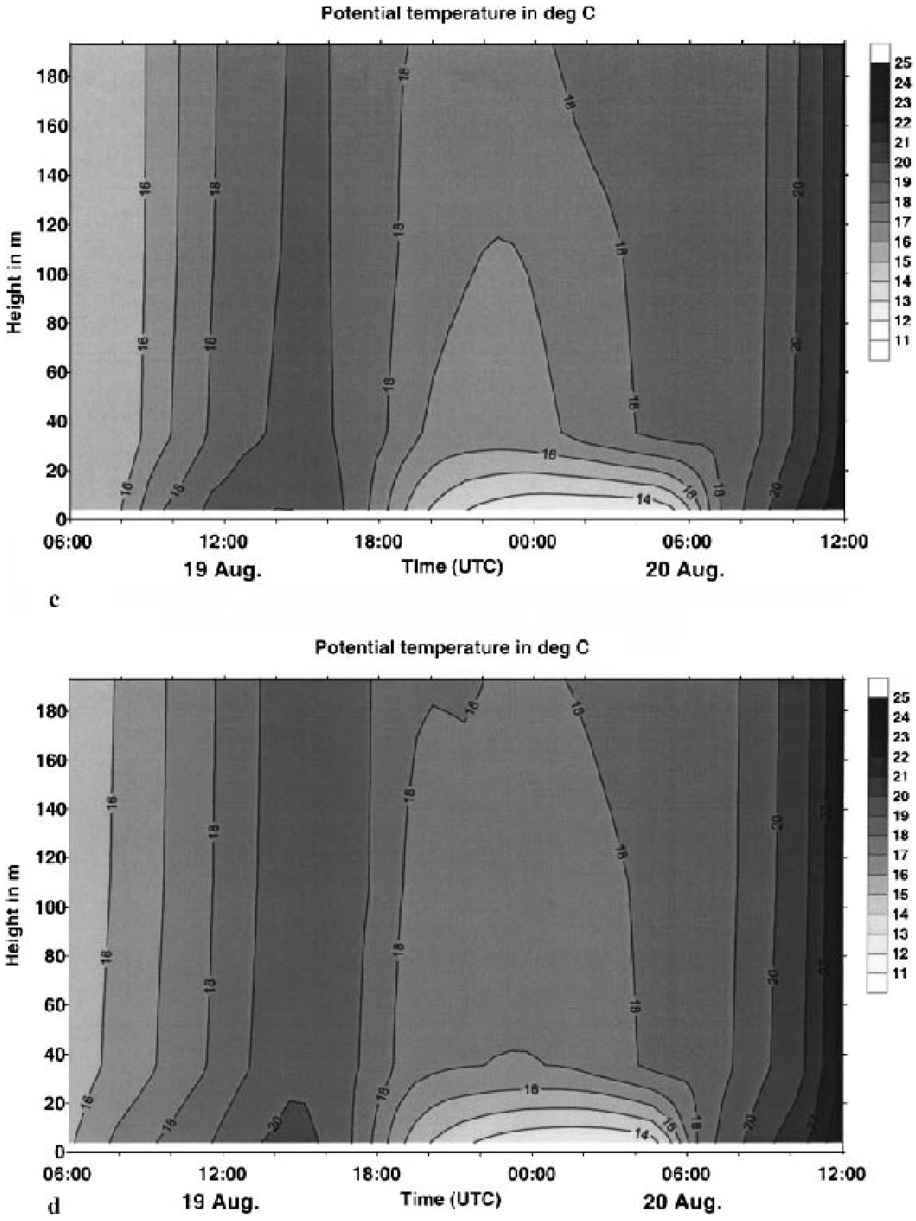

Fig. 24 (*continued*)

higher soil moisture leads to a decreased heating of the boundary layer during daytime with maximum temperatures being 3–4 °C lower than in the control run or the measurements. Minimum values during the night are 2–3 °C lower compared to the control run, but the surface inversion strength is similar. The increased evapotranspiration also results in a moistening of the boundary layer (not shown). Despite of these improvements, the modelled boundary-layer structures are still not satisfactory and even worse than the control run when compared to the measured conditions. An intercomparison of the boundary layer height (not shown) between radiosonde measurements and model simulations shows a good agreement for the control run (boundary-layer height of about 1300 m). In contrast, a too shallow boundary layer (800 m) is found in the model runs with increased soil moisture. Thus we can conclude that the model simulations produce much better results for the boundary layer conditions in the dryer model runs than in the moister ones. For the energy fluxes at the ground it seems to be just the opposite. The energy fluxes are much more realistic in the model runs with increased soil moisture than in the runs without artificially increased soil moisture.

6. Summary and outlook

We have presented a method to calculate regional evapotranspiration by means of assimilating observational data into the LM of the DWD. Evapotranspiration depends strongly on soil moisture and available energy at the surface, and therefore on precipitation and insolation. Current mesoscale models, however, do not yet predict cloudiness and precipitation with sufficient quality. To account for this problem we assimilate both parameters into the SVAT module of the LM. The assimilation of precipitation is based on radar measurements while solar radiation is derived from METEOSAT data. Three cases have been studied in order to quantify the influence of the assimilation on the evapotranspiration process as well as to validate the model results with ground-based measurements of the turbulent fluxes and the boundary layer structure within a fruit orchard.

The case studies have shown that the simulated surface energy fluxes are strongly modified by the assimilation. In the case of a heavy rainfall event, where the model forecast for cloudiness and precipitation differs considerably from reality, large differences are found in the spatial distribution, temporal development and total amount of evapotranspiration between the control run and the model with the assimilation of both precipitation and solar radiation. But also for a case study, in which the model simulates the general weather situation quite well, the differences between simulated evapotranspiration of control and assimilation runs are large and can be traced to different insolation and temporal displacements of precipitation events. In the considered cases the effect of the assimilation of both rainfall and radiation is dominated by the solar radiation.

With regard to the assimilation of precipitation and solar radiation it has to be taken into account that both derived rainfall information and insolation using radar and METEOSAT data, respectively, include uncertainties. The accuracy of the radar measurements is restricted by e.g. calibration and clutter. Furthermore, measured radar reflectivities have to be converted to rain rates, which is done using a standard Z-R relationship according to Marshall et al. (1954). A variation of this relation, which can be observed due to modifications of types and size distributions of hydrometeors, is ignored. Thus the derived rain rates can only be considered as "ground truth" within certain limitations. When METEOSAT VIS data are used to calculate insolation, a first error occurs due to the fact that this channel is not calibrated after launch. Thus information from a pre-launch calibration has to be used to convert measured counts into reflectivities. In addition, the radiation transfer scheme of McNider et al. (1995), which is used to calculate solar radiation, is quite simple and includes several assumptions within the parameterizations. Nevertheless, the amount and especially the temporal development and spatial distribution of derived precipitation and solar radiation are by far better than the ones simulated by the model. Therefore the assimilation of these parameters into the SVAT module has a positive effect on the simulated distribution of evapotranspiration despite the uncertainties of the measurements.

The validation of the model results focussed on the temporal development of the turbulent fluxes and the structure of the boundary layer. The different techniques used to determine evapotranspiration (Bowen ratio method, direct flux and sap flow measurements) yield similar results giving us confidence in the validation data. The observations point out quite severe shortcomings of the model simulation. During the night the modelled net radiation is much lower than the observed one because of too high near-surface temperatures. Furthermore the measured and simulated daily courses of latent and sensible heat fluxes behave diametrically different. The observations show a Bowen ratio of approximately 0.5 during daytime while the model simulates values of about 2. A possible explanation is the low soil moisture content of the initial model fields. Increasing the soil moisture content artificially by 50% or 100% leads to a significantly better representation of the turbulent fluxes in the LM. This increase, however, results in a considerably reduced heating of the boundary layer so that the maximum temperatures in the lower daytime boundary layer are predicted too low. In this case the assimilation of solar radiation and precipitation causes only minor improvements. In order to avoid a soil to dry down it is possible to run the soil model TERRA as a stand alone model forced by remotely sensed data a couple of months in advance. The calculated soil moisture can then be used to initialize the LM for the considered time periods. TERRA, however, does not consider the lateral transport of water within the soil so that the resulting soil moisture would not be very realistic. Another possible reason for the inadequate prediction of the turbulent fluxes could be the crude representation of vegetation within the SVAT module of the LM. This emphasizes the need of implementing a more complex SVAT module in the LM for future simulation studies.

While the validation presented here focusses on the temporal variability of the surface fluxes and the boundary layer structure, future studies including airborne and satellite observations aim at the validation of the spatial heterogeneity of the turbulent fluxes (see Fig. 1). Turbulence and remote sensing measurements from an aircraft-based experiment in May 1999 in the NRB will allow a comparison with model results over areas with extensions of several grid points. Surface radiation temperatures by satellites will give a large-scale validation of the SVAT module. In the future we will couple the LM with a hydrological model in order to validate the water balance on larger time scales.

Acknowledgements

The work was supported by the Deutsche Forschungsgemeinschaft as part of the SFB 350 (TP A4). We also gratefully acknowledge the support by the German Weather Service (DWD) by providing the mesoscale model "Lokal-Modell" and the radar data. The model runs were performed on the Cray J90 of the DWD. The METEOSAT data were provided by Eumetsat. The authors wish to thank all persons who supported and took an active part in the 1998 measurement campaign. Special thanks go to the staff of the Obstversuchsgut Klein-Altendorf. Especially acknowledged is the invaluable help of many students and colleagues of the Meteorogical Institute of the University of Bonn, without whose assistance the measurements would hardly have been possible.

References

Bowen IS (1926) The ratio of heat losses by conduction and by evaporation from any water surface. Phys Rev 27: 779–787

Braun P, Schmid J (1999) Sap flow measurements in grapevines (Vitis vinifera L.) 1. Stem morphology and use of the heat balance method. Plant Soil 215: 39–45

Davies HC (1976) A lateral boundary formulation for multi-level prediction models. Quart J R Meteor Soc 102: 405–418

Doms G, Schättler U (1999) The non-hydrostatic limited-area model LM (Lokal-Modell) of the DWD, available from Deutscher Wetterdienst, D-63004 Offenbach, Germany, 180 pp

Drüen B, Heinemann G (1998) Rain rate estimation from a synergetic use of SSM/I, AVHRR and meso-scale numerical model data. Meteor Atmosph Phys 66: 65–85

Eymard L, Taconet O (1995) The methods for inferring surface fluxes from satellite data, and their use for atmosphere model validation. Int J Remote Sens 16: 1907–1930

Foken T, Wichura B (1996) Tools for quality assessment of surface-based flux measurements. Agr For Meteor 78: 83–105

Jacobsen I, Heise E (1982) A new economic method for the computation of the surface temperature in numerical models. Beitr Phys Atmosph 55: 128–141

Louis J-F (1979) A parametric model of vertical eddy fluxes in the atmosphere. Bound Layer Meteor 17: 187–202

Marshall JS, Hitschfeld W, Gunn KLS (1954) Advances in radar weather. Adv In Geophys 2: 1–56

McNider RT, Song JA, Kidder SQ (1995) Assimilation of GOES derived solar insolation into a mesoscale model for studies of cloud shading effects. Int J Rem Sens 16: 2207–2231

Mellor GL, Yamada T (1974) A hierarchy of turbulence closure models for planetary boundary layers. J Atmos Sci 31: 1791–1806

Pelgrum H, Bastiaanssen WGM (1996) An intercomparison of techniques to determine the area-averaged latent heat flux from individual in situ observations: A remote sensing approach using the European Field Experiment in a desertification-threatened area data. Water Resour Res 32: 2775–2786

Reudenbach C, Heinemann G, Heuel E, Bendix J, Winiger M (2000) Investigation of summertime convective rainfall in Western Europe based on a synergy of remote sensing data and numerical models. Meteorol Atmos Phys, this issue

Ritter B, Geleyn J-F (1992) A comprehensive radiation scheme for numerical weather prediction models with potential applications in climate simulations. Mon Wea Rev 120: 303–325

Sakuratani T (1981) A heat balance method for measuring water flux in the stem of intact plants. J Agric Meteorol 37: 9–17

Svensson K (1997) Aufbau einer Anlage für Turbulenzmessungen nach der Eddy-Korrelationsmethode, Diplomarbeit, Meteorologisches Institut, University of Bonn, 94 pp

Tiedtke M (1989) A comprehensive mass flux scheme for cumulus parameterization in large-scale models. Mon Wea Rev 117: 1779–1800

Weibel FP, Vos JAd (1994) Transpiration measurements on apple trees with an improved stem heat balance method. Plant Soil 166: 203–219

Authors' addresses: P. Braun, The Royal Veterinary and Agricultural University, Dept. of Agric. Sci, Sect. Horticulture, Agrovej 10, DK-2630 Taastrup, Denmark. (E-mail: pbr@kvl.dk); B. Maurer, G. Müller, P. Gross, G. Heinemann and C. Simmer, Meteorological Institute, University of Bonn, Bonn, Germany